Skillful Subseasonal Prediction of U.S. Extreme Warm Days and Standardized Precipitation Index in Boreal Summer

DOUGLAS E. MILLER,[a] ZHUO WANG,[a] BO LI,[b] DANIEL S. HARNOS,[c] AND TRENT FORD[d]

[a] *Department of Atmospheric Sciences, University of Illinois at Urbana–Champaign, Urbana, Illinois*
[b] *Department of Statistics, University of Illinois at Urbana–Champaign, Urbana, Illinois*
[c] *NOAA/NCEP/NWS/Climate Prediction Center, College Park, Maryland*
[d] *Illinois State Water Survey, Prairie Research Institute, University of Illinois at Urbana–Champaign, Urbana, Illinois*

(Manuscript received 13 November 2020, in final form 20 April 2021)

ABSTRACT: Skillful subseasonal prediction of extreme heat and precipitation greatly benefits multiple sectors, including water management, public health, and agriculture, in mitigating the impact of extreme events. A statistical model is developed to predict the weekly frequency of extreme warm days and 14-day standardized precipitation index (SPI) during boreal summer in the United States. We use a leading principal component of U.S. soil moisture and an index based on the North Pacific sea surface temperature (SST) as predictors. The model outperforms the NCEP Climate Forecast System, version 2 (CFSv2), at weeks 3–4 in the eastern United States. It is found that the North Pacific SST anomalies persist for several weeks and are associated with a persistent wave train pattern, which leads to increased occurrences of blocking and extreme temperature over the eastern United States. Extreme dry soil moisture conditions persist into week 4 and are associated with an increase in sensible heat flux and a decrease in latent heat flux, which may help to maintain the overlying anticyclone. The clear-sky conditions associated with blocking anticyclones further decrease soil moisture and increase the frequency of extreme warm days. This skillful statistical model has the potential to aid in irrigation scheduling, crop planning, and reservoir operation and to provide mitigation of impacts from extreme heat events.

KEYWORDS: Atmosphere–land interaction; Atmosphere–ocean interaction; Blocking; Extreme events; Climate variability; Soil moisture; Statistical forecasting

1. Introduction

Subseasonal prediction lies between synoptic weather forecasting and seasonal prediction. The former is strongly influenced by initial conditions while the latter is more impacted by slowly evolving components of the climate system, such as the ocean and land conditions, which act as ''boundary conditions'' for the atmospheric evolution (National Academies of Sciences Engineering and Medicine 2016). Subseasonal prediction has long been defined as a ''predictability desert'' and has the potential to provide important information for the health, water management, and agriculture sectors to mitigate the destructive impacts of extreme events, especially when the frequency of some extreme events, such as heat waves, is projected to increase in a warming climate (Meehl and Tebaldi 2004; Teng et al. 2016).

Various sources of predictability act to enhance prediction skill of midlatitude weather, including El Niño–Southern Oscillation (ENSO) and the Madden–Julian oscillation (MJO; Qin and Robinson 1995; Jones et al. 2004). However, these patterns of variability prevail during the winter season and additional predictability sources are needed during summer. Multiple studies have examined the ability for operational forecast models to predict aspects of extreme heat at the subseasonal to seasonal (S2S) time scales. Pepler et al. (2015) demonstrated the prediction of the summer (JJA) seasonal mean, the 10th-percentile, and the 90th-percentile daily surface temperatures using a multimodel ensemble. Large prediction skill of the summer mean temperatures exists mainly over oceans in the Northern Hemisphere. Although the skill in forecasting the seasonal mean is generally higher than the skill for extremes, there is slightly greater skill, albeit nonsignificant, in predicting the 90th-percentile temperature (defined as the 90th percentile of maximum temperature for each month, averaged over a season) over the western United States than the summer mean temperatures. Slater et al. (2019) examined the skill of the North American Multi-Model Ensemble (NMME) in predicting surface air temperatures over the United States and showed that most models suffer from unconditional biases during the summer season. Tian et al. (2017) examined the ability of the Climate Forecast System, version 2 (CFSv2), to predict the number of extreme warm days (EWDs) over 7-day, 14-day, and 30-day periods. The average Heidke skill score (HSS) for the 7-day prediction window over the continental United States (CONUS) was between 30 and 40 at week 1 and dropped to ~10 at week 4. Despite the low HSS, the CFSv2 was able to predict anomalous warm temperatures on the subseasonal time scale associated with the 2012 U.S. Great Plains flash drought (DeAngelis et al. 2020).

The relationship between soil moisture and extreme temperature is well known (Diffenbaugh et al. 2007; Seneviratne et al. 2010; Hirschi et al. 2011), and the importance of soil conditions in

Supplemental information related to this paper is available at the Journals Online website: https://doi.org/10.1175/10.1175/JCLI-D-20-0878.s1.

Corresponding author: Douglas E. Miller, dmiller23@niu.edu

DOI: 10.1175/JCLI-D-20-0878.1

long-range surface air temperature prediction was emphasized early on (Namias 1952). Specifically, an inverse relationship has been demonstrated between soil moisture and the surface air temperature in subsequent months in large areas of the United States during summer (Huang et al. 1996). Huang and colleagues noted that the soil moisture is a better local predictor for temperature than precipitation, as soil moisture has longer memory. Mueller and Seneviratne (2012) demonstrated increased probability of EWDs following dry periods, noting the value of soil moisture initialization in operational models. Koster et al. (2014, 2016) demonstrated that localized regions of dryness in the central United States can lead to a significant change in precipitation and extreme temperature in remote regions during June and July using a stationary wave model and an atmospheric general circulation model. Orth and Seneviratne (2014) derived soil moisture forecasts from a simple water balance model, and then predicted extreme temperature for over 400 stations in Europe using a simple linear relationship between soil moisture and temperature. They achieved skill greater than climatology at lead times up to 2 weeks, with skill at weeks 3 and 4 in certain locations. Some stations showed improvements of skill over the ECMWF forecast model at weeks 3 and 4, highlighting the potential for more skillful temperature forecasts by dynamic models through a more effective use of soil moisture information. In short, the long-lasting memory of soil moisture makes it a valuable predictability source for surface temperature on the subseasonal time scale.

The slowly evolving nature of sea surface temperature (SST) has also been exploited for S2S prediction of temperature and precipitation. Specifically, previous studies have shown that midlatitude North Pacific SST anomalies precede U.S. heatwave events (Namias 1982; Lyon and Dole 1995). Alfaro et al. (2006) used canonical correlation analysis of the North Pacific Ocean SST to predict the seasonal maximum and minimum temperatures. More recently, McKinnon et al. (2016) investigated the predictability of eastern U.S. hot days and found significant precursor anomalies of the North Pacific SST 50 days before extreme hot days. Additionally, Namias (1982) found that a large cold ocean anomaly in the North Pacific influenced the formation of the east Pacific ridge and preceded the Great Plains drought of summer 1980.

Here, we aim to develop skillful statistical prediction of extreme heat and precipitation in boreal summer on the time scale of 3–4 weeks, which remains a challenging task for operational numerical models. We will demonstrate the importance of SST and soil moisture in influencing extreme events over the eastern United States. Section 2 describes the data and methods. The prediction skill of the statistical model is presented in section 3, while the underlying physical mechanisms linking the predictors and extreme weather are examined in section 4. Section 5 contains the discussion and conclusions.

2. Data and method

a. Data

The observational data consists of 2-m temperature (T2m), precipitation, SST, soil moisture within the top 28 cm, 500-hPa geopotential height (Z500), and sensible heat flux from the ERA-Interim reanalysis (ERAI; Dee et al. 2011) dataset. Data are interpolated to a 1° latitude–longitude grid from a T255L60 (~0.7° in the horizontal plane) grid. The ERAI SST field is constructed from various SST datasets, including the Operational Sea Surface Temperature and Sea Ice Analysis (OSTIA; Dee et al. 2011), and has comparable lead–lag relationships between SST and precipitation to the NCDC dataset (Kumar et al. 2013). The precipitation is produced from ECMWF Integrated Forecast System (Cy31r2) forecast model and is comparable to the Global Precipitation Climatology Project (GPCP) V2.1 (Balsamo et al. 2010). Li et al. (2020) showed that the ERAI soil moisture has statistically significant correlations with observations. Although a finer-resolution observational dataset may be more useful if one focuses on local values of soil moisture, the ERAI data are satisfactory for our purpose of examining large-scale variability in soil moisture.

The skill of our statistical model is compared with the skill of the NCEP CFSv2 (Saha et al. 2014). The reforecast data contain four ensemble members and are initialized daily from 1999–2010 on an ~1° grid (L64). It contains forecasts out to 44 days. The reforecasts of T2m and precipitation are used to identify extreme events in the CFSv2. Our statistical model is evaluated over 1999–2010 to be consistent with the reforecast time period; a longer time period, 1980–2017, is chosen to ensure the robustness of results when examining the link between the predictors and extremes. It is also shown that the statistical model contains skill when evaluated over the longer time period. We focus on the month of July, but the findings are qualitatively valid for the other summer months as well.

b. Two-dimensional blocking index

To provide a dynamical mechanism for the increased frequency of EWDs, we calculate a two-dimensional blocking index following a standard deviation approach (R. L. Miller et al. 2020). We first detrend the Z500 field from 1980–2017 at each grid point and then apply an inverse sine-of-latitude weight ($\sin 45^\circ/\sin\phi$) to better represent atmospheric energy dispersion by eliminating bias toward high latitudes (Hoskins et al. 1977; Dole and Gordon 1983). A 5-day running mean is then calculated to remove high-frequency fluctuations. On each calendar day and for each grid point, the standard deviation is calculated within a 29-day period centered on that calendar day from 1980–2017 (or 1999–2010 for the CFSv2). We then mark grid points that exceed 1.5 times the local standard deviation. To be considered a blocking event, the area of an extreme anomaly must be greater than $10^\circ \times 10^\circ$ (100 grid points) and persist for at least 5 days. We then smooth the blocking frequency by averaging over a $5^\circ \times 5^\circ$ box at each grid point. The climatology of this blocking algorithm is shown in Fig. S1 in the online supplemental material.

c. Extreme warm days, standardized precipitation index, and predictors

This study aims to predict the number of EWDs per week and 14-day standardized precipitation index (SPI) with a focus on weeks 3 and 4. Here, EWDs are defined as a day with a detrended daily average temperature greater than the 90th

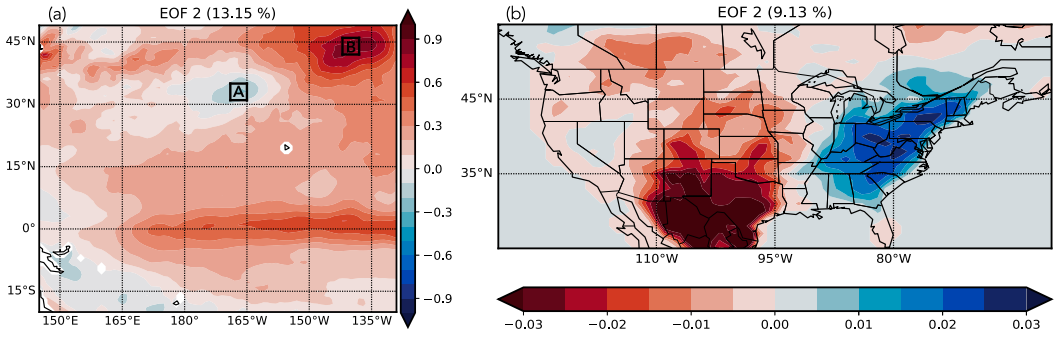

FIG. 1. (a) The second EOF mode of daily SST in July over 20°S–50°N, 145°E–128°W. The North Pacific SST index was calculated by subtracting the average over box B (42°–46°N, 142°–138°W) from the average over box A (31°–35°N, 169°–165°W). (b) The second EOF mode of U.S. soil moisture during July. The numbers in the title represent the variance explained. Note that the color bar is reversed for soil moisture so that red indicates dry conditions and blue indicates moist conditions.

percentile of all July and August days from 1980 to 2017 at each grid point (Miller and Wang 2019). The field is smoothed by averaging a 5° × 5° box centered at each grid point.

The SPI, developed by McKee et al. (1993), is a widely used index for meteorological drought. The SPI is calculated by fitting a gamma function to the accumulated precipitation distribution, followed by transformation to a normal distribution. It can be interpreted as the number of standard deviations from the mean. For example, a SPI value below −1 is considered dry while a value below −2 is extremely dry. The SPI can be calculated for different periods, ranging from 1 to 36 months, but can be used on shorter time scales. Here, we calculate the SPI using the 14-day accumulated precipitation within a 10° × 10° box. A coarse spatial resolution and a long time interval are chosen to reduce the number of low precipitation events and facilitate the transformation from a gamma distribution to a normal distribution.

Similar to the ERAI, an EWD for the CFSv2 is defined as a day with a daily mean temperature greater than the 90th percentile of detrended daily mean temperatures for all lead times initialized in July during 1999–2010. The 90th percentile is calculated separately for each ensemble member. The same method for SPI is applied to the CFSv2. Since the SPI is calculated over a 14-day period, week 3–4 is the period of days 14–28 and week 4–5 is the period of days 21–35.

Previous studies showed that anomalous SSTs over the North Pacific precede U.S. extreme heat events (Namias 1982; Lyon and Dole 1995; McKinnon et al. 2016). To objectively define a SST index over the North Pacific, we first perform empirical orthogonal function (EOF) analysis on the July daily Pacific SST field (20°S–50°N, 145°–232°E). The leading mode displays the well-known ENSO pattern with strong SST anomalies in the tropical Pacific and anomalies of the opposite polarity in the extratropical central Pacific (Fig. S2 in the online supplemental material). The second leading mode of Pacific SST (Fig. 1a) displays a North Pacific dipole pattern, similar to the patterns related to heat wave events reported in previous studies (Namias 1982; McKinnon et al. 2016). Here, we define a simple SST index (denoted as the NPSST index) as the difference between the areal average of the northern node (42°–46°N, 142°–138°W) and the areal average of the southern node (31°–35°N, 169°–165°W). The pentad mean of the NPSST index is used as a predictor in our statistical model. Our July mean NPSST index is strongly correlated (Pearson correlation coefficient $r = 0.6$; p value ≈ 0) to the July Pacific meridional mode. Strong SST anomalies in the tropical Pacific are also evident in the second EOF that resemble the ENSO but are shifted eastward relative to the leading EOF mode. Although previous studies have shown more extreme heat events during La Niña summers (Loikith and Broccoli 2014; Luo and Lau 2020), Niño-3.4 is not included as a predictor because the NPSST index and the Niño-3.4 index are significantly correlated (p value < 0.01). However, the Niño-3.4 index was tested and the NPSST produced more skillful predictions.

Our second predictor is defined based on July soil moisture anomalies over the United States. We perform EOF analysis on the top two layers of daily ERAI soil moisture (0–28 cm). The first four principal components (PCs; Fig. S3 in the online supplemental material) are examined separately, and we find that the second EOF mode has a stronger correlation with temperature and precipitation over the eastern United States than the other modes, and it is thus chosen as the second predictor. As shown in Fig. 1b, the second EOF mode represents positive soil moisture anomalies over the eastern United States and negative soil moisture anomalies over the southern plains and northern Mexico.

It is worth mentioning that the two predictors do not have a consistent correlation throughout the 38 years of analysis (not shown), and the correlation of the daily time series of the predictors in July fluctuates between positive and negative values from year to year. In addition, we focus on predictions initialized in July, but week 3–4 forecasts and composite analysis with a lag of 3–4 weeks extends into August.

d. Model evaluation and statistical significance

A multiple linear regression (MLR) model is used to predict the weekly frequency of EWDs (i.e., the number of EWDs per week) and the 14-day SPI, and the leave-one-year-out cross-validation method is used to assess the prediction skill. With leaving one year out, the training dataset contains 1147 time

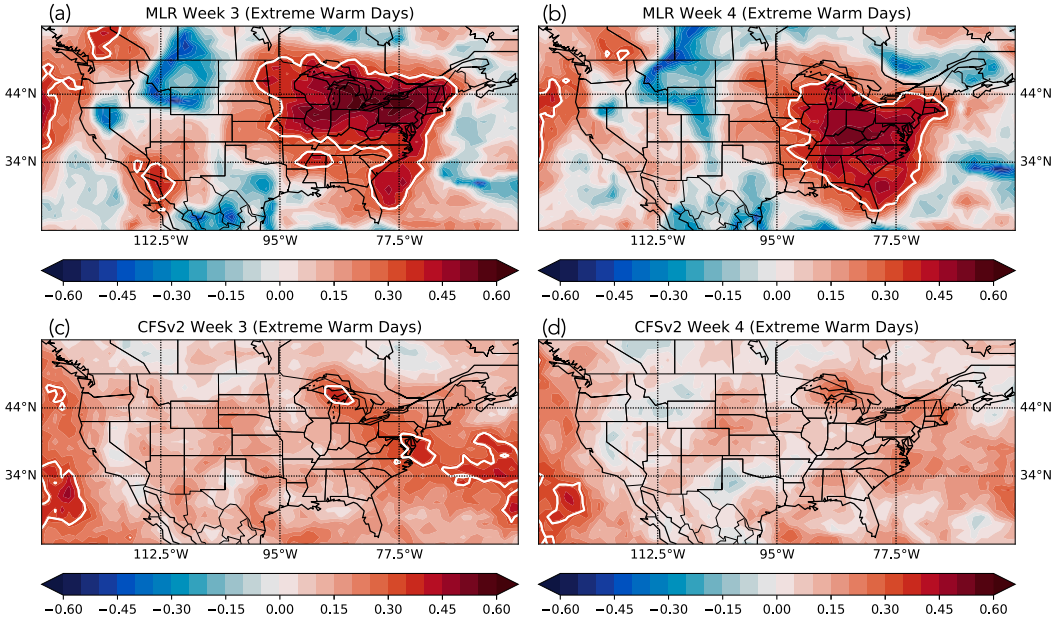

FIG. 2. Heidke skill score between the (a),(b) MLR-predicted or (c),(d) CFSv2-predicted extreme warm days per week and observations at weeks (left) 3 and (right) 4. White contours indicate HSS greater than 0.33, or a forecast that is correct 2 times as often as it is incorrect.

points (37 years × 31 days per year), and the test dataset includes 31 time points (i.e., one month). The evaluation period spans 1999–2010 to be consistent with the CFSv2 model years, but it is shown that the statistical model performs well when evaluated over the observational time period (1980–2017: see section 3a). To evaluate the prediction model, we calculate the Heidke skill score (HSS; Wilks 2011) for two-tier prediction between the observed and predicted frequency of EWDs or SPI. The threshold to separate the tiers is the median of the respective datasets. To further evaluate the model, we calculate the critical success index (CSI), probability of detection (POD), and the probability of false detection (POFD). A skillful forecast will have a high HSS, CSI, and POD while showcasing lower values of POFD. The Spearman rank correlation is also presented in supporting information to show the skill of the deterministic forecasts.

In addition to the MLR, a generalized additive model (GAM) was tested, which can incorporate the nonlinear forms of predictors. The GAM model provides a better fit than the MLR (Fig. S4 in the online supplemental material), with overall larger correlation coefficients across the United States. However, when the GAM model is used on independent data, the model fails to perform as well as the MLR model (Fig. S5 in the online supplemental material). This is not surprising because GAM, when treated as a completely nonparametric model, is more flexible than a linear model but will inherit the potential poor prediction skill of smoothing spline models. This leads to better model fitting as shown in Fig. S4, but poor prediction as shown in Fig. S5. The lower skill and increased computational cost of GAM encourage us to move forward with the MLR instead of the GAM.

Composite anomalies of various variables are examined to investigate the mechanisms linking temperature and SPI extremes and the predictors. As our predictor values represent slowly evolving components of the Earth system, extreme values of the indices will likely cluster together during certain years. To avoid overlapping events, the composites are constructed so that an event occurs when the indices first become extreme (i.e., exceeding a threshold) and a second event may not occur until 28 days later. To test the significance of the anomalies of Z500, SST, sensible heat flux, and SPI, a two-tailed Student's t test is performed with a null hypothesis that the anomalies do not differ from zero. A Mann–Whitney U test is used to test the significance of the composite anomalies of EWDs per week, soil moisture, and the weekly blocking frequency as the distributions are non-Gaussian.

3. Statistical prediction of extreme warm day frequency and 14-day SPI

a. *Predicting the weekly frequency of EWDs*

Figures 2a and 2b present the HSS of the MLR model in predicting weekly frequency of EWDs at weeks 3 and 4. The MLR model (Figs. 2a,b) exhibits large positive HSS values over the eastern United States, indicating a forecast that is more skillful than climatology. A large portion of the skillfully predicted area contains HSS values greater than 0.33 at weeks 3 and 4 over a large region in the eastern United States, signifying a two-tier prediction that is correct twice as often as it is incorrect. HSS values reach as high as 0.60 at week 3 and 0.54 at week 4. To complement the HSS, we also investigate the

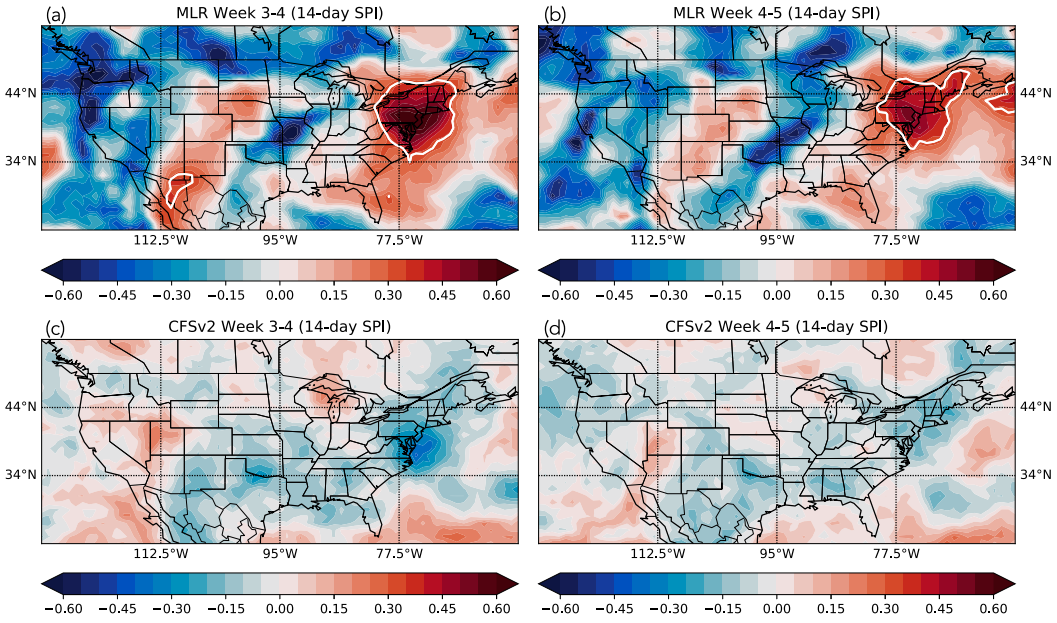

FIG. 3. As in Fig. 2, but for 14-day SPI.

CSI, POD, and POFD at week 4 (Fig. S6 in the online supplemental material). The MLR model contains CSI values greater than 50% over the eastern United States, indicating that more than half of the observed and/or predicted extreme warm events were correctly forecast. In addition, a large portion of the eastern United States contains a hit rate (POD) of greater than 70% and a false alarm rate (POFD) of less than 30%. Evaluation of the deterministic forecasts also produces large and significant Spearman rank correlations (Fig. S7 in the online supplemental material) between the statistical forecasts and observations. Although the above results are for the period 1999–2010, the model still contains positive HSSs and hit rates greater than 60% over the eastern United States when evaluated over 1980–2017 (Fig. S8 in the online supplemental material). Most skillfully predicted individual events (correct positives and correct negatives) over the eastern United States are associated with strong anomalies of the NPSST index and/or soil moisture predictor (Fig. S9 in the online supplemental material). The negative soil index values correspond to abnormally dry conditions over the eastern United States, while the negative NPSST index values correspond to a wave train that produces an anticyclone over the eastern United States. The relationship between the predictors and extreme warm days are further discussed in section 4.

The CFSv2 exhibits large HSS at week 1 and week 2 (not shown), but the skill decreases rapidly with increasing forecast lead times. Although the CFSv2 shows a larger area of positive HSS at week 3, the HSS hardly exceeds 0.15 at week 3 and further decays at week 4 (Figs. 2c,d). The CFSv2 also contains negative values of CSI at week 4 along with POD and POFD values of 50%, indicating little skill at this lead time (Fig. S10 in the online supplemental material). The MLR model is more skillful than the CFSv2 over the majority of the eastern United States at both weeks 3 and 4.

b. *Predicting 14-day standardized precipitation index*

The 14-day SPI prediction skill is presented in Fig. 3. As expected, the MLR model prediction skill of SPI is overall much less than that of the EWD frequency (Figs. 2a,b). Two locations of positive HSSs exist: one over the North American monsoon region (Adams and Comrie 1997) that extends into the northern plains and the other over the east coast of the United States with the maximum HSS over the northeastern United States. The skill over western Mexico decreases from weeks 3–4 to weeks 4–5, while strong skill maintains from weeks 3–4 to weeks 4–5 in the northeast, with the HSS values exceeding 0.6 in some locations. Interestingly, the MLR model contains a POD greater than 80% and a POFD less than 20% over a small region in the northeast (Fig. S11 in the online supplemental material). In contrast, the CFSv2 is hardly skillful at weeks 3–4 or weeks 4–5 (Figs. 3c,d), as negative HSSs are evident across the United States.

4. Underlying physical mechanisms for the statistical prediction

a. *North Pacific SST predictor*

Composite analysis is performed to investigate the underlying physical mechanisms related to the two predictors used in the MLR model. The lead–lag composite anomalies in Fig. 4 are constructed based on days when the NPSST index first becomes less than the 10th percentile (12 events over 1980–2017). The 10th percentile is chosen due to the inverse relationship between the NPSST index and the EWD frequency over the eastern United States.

A wave train is evident extending from the Eurasian continent to the North Atlantic. It consists of anomalous highs over Asia, the western North Pacific, and North America during

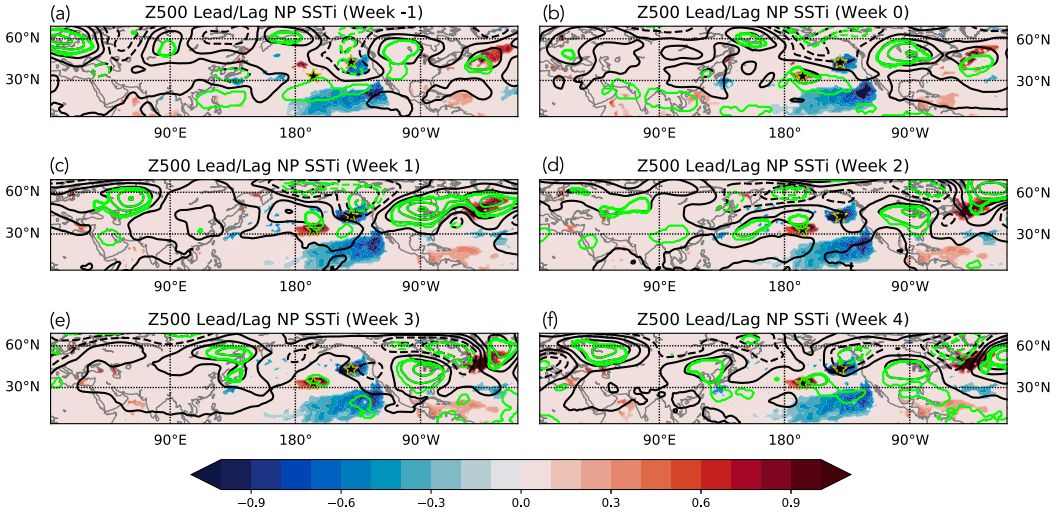

FIG. 4. Lead–lag composites of Z500 (contours from −60 to 60 m every 15 m) and SST (shading) from week −1 to week 4 based on when the NP SST index first becomes less than the 10th percentile (12 events over 1980–2017). To prevent overlap, an event cannot occur within 4 weeks of another event. From day −14 to day −7 is week −1, from day −7 to day 0 refers to simultaneous composites (week 0), week 1 is from day 1 to day 7, etc. Only significant SST anomalies are shown (5% significance level), and green contours represent Z500 anomalies exceeding the 5% significance level. Black stars with gold outline indicate locations used in calculation of the NPSST index.

week 0, resembling a circumglobal teleconnection pattern (Ding and Wang 2005; Teng and Branstator 2017). The wave train evolves slowly from week −1 to week 1, with the major centers of action remaining quasi-stationary, especially the anticyclone over the United States. From week 2 to week 3, the upstream cells of the wave train over the Eurasian continent weaken. While the wave train remains prominent from the North Pacific to the North Atlantic Ocean, the anomalous high over North America shifts southward in week 2, and then remains over the eastern United States from week 3 to week 4. During the 6-week period, negative SST anomalies prevail over the northeast Pacific, with small regions of positive SST anomalies over the central North Pacific (including box A in Fig. 1a). The pattern closely resembles the EOF2 pattern of SST shown in Fig. 1a (but with an opposite polarity) and is also similar to the composite SST patterns in McKinnon et al. (2016).

The circulation anomalies over North America are associated with extreme weather conditions (Fig. 5). Blocking frequency increases significantly in the region of the anomalous high, first located along 45°N over the northern United States in week 1. The blocking anticyclone then slightly shifts southeastward and remains over the eastern United States at weeks 3 and 4. The increase in blocking frequency due to the wave train contributes to subsidence and increased solar radiation and alters the surface energy budget (Brunner et al. 2017; Pfahl and Wernli 2012). Specifically, our results show a decrease in soil moisture and an increase in the surface sensible heat flux throughout the 4-week period (not shown). Resulting from the blocking anticyclone, there is a significant increase in EWDs per week centered in the eastern half of the United States at weeks 3 and 4, as well as a significant decrease in precipitation (negative SPI) (Fig. 5). A MLR model was developed to predict the blocking frequency using the NPSST as the predictor. It shows large positive HSS values over the Midwest region and far larger skill than the CFSv2 at weeks 3–4 (Fig. 6), which is remarkable considering the difficulty operational models have in predicting blocking regimes (Ferranti et al. 2015).

Given that a well-defined wave train pattern exists in week −1 (Fig. 4a), it is possible that the SST anomalies are excited by the overlying circulation, although the SST anomalies may aide in maintaining the wave train through air–sea interaction (Seager et al. 2003). Using atmospheric general circulation model simulations, Teng and Branstator (2017) suggested that a circumglobal wave train pattern would precede U.S. heat waves by 15–20 days. The lead–lag composites in Fig. 4 suggest that a longer lead can be identified. We defined a daily wave train index using Z500 (WTZ500) based on the regions of significant correlations (Fig. S12 in the online supplemental material) between the NPSST index and Z500 at week 0 (from day −6 to day 0). Specifically, the index is calculated by adding areal averages of Z500 over the central Pacific (32°–36°N, 165°–161°W) and north central United States (44°–48°N, 95°–90°W), followed by subtracting an areal average of Z500 over the northeast Pacific (48°–52°N, 132°–128°W). We attempt predicting the EWDs using the WTZ500 index. However, it fails to produce as skillful of a prediction as the NPSST index. The lack of skill is likely because the impacts of the wave train not only depend on its intensity but also its persistence: only persistent wave trains can induce the dipole SST anomalies over the North Pacific and extreme conditions over the United States. This is supported by the analysis in Fig. 7.

Figure 7 shows similar composites as Fig. 4, except that the composites are constructed for two subgroups: persistent wave train events with the WTZ500 index exceeding 1.0 standard deviation for at least five days during week 0, and nonpersistent

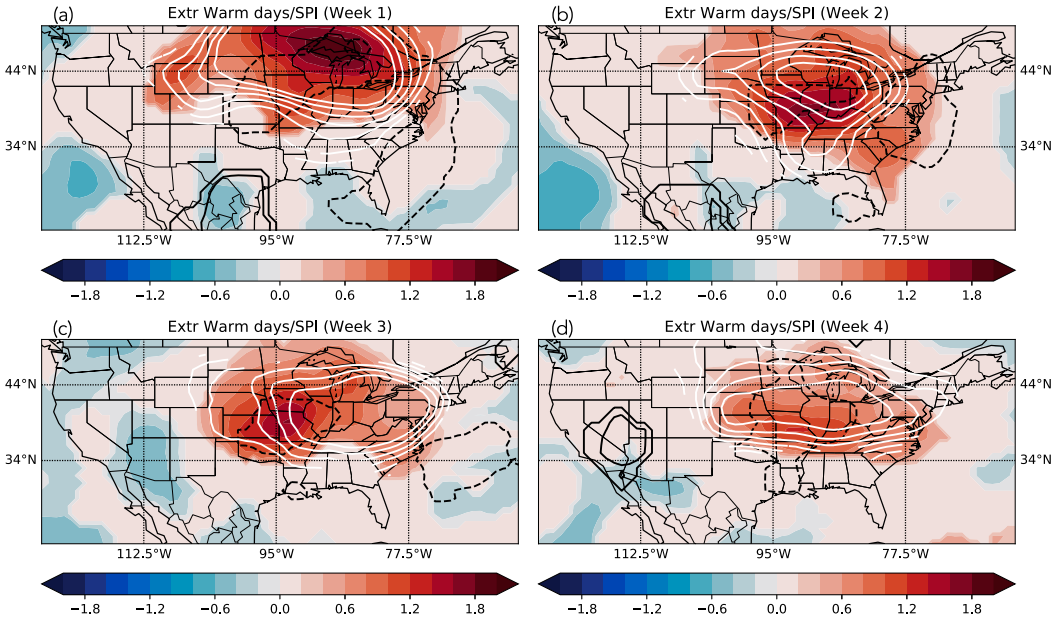

FIG. 5. Composites of extreme warm days per week (shading), 14-day SPI (black contours from −2 to 2 days every 0.5 days), and blocking-frequency anomalies (white contours from −2 to 2 days every 0.25 days) at weeks (a) 1, (c) 2, (e) 3, and (g) 4. Composites are calculated based on when the NPSST index first becomes less than the 10th percentile. To prevent overlap, an event cannot occur within 4 weeks of another event (12 events over 1979–2017). Only significant anomalies are shown ($\alpha = 0.05$).

wave train events with the WTZ500 index exceeding 1.0 standard deviation for at least one day but no more than four days in week 0. The contrast between the two subgroups is intriguing. The North Pacific SST patterns associated with the persistent wave train project onto the second EOF of Pacific SST (Fig. 1a) and weaken throughout the 4-week period, while the nonpersistent wave train events show little significant SST anomalies, suggesting the nonlinearity of the WTZ500 impacts on SST. At week 0, the circulation patterns are similar between the two groups over the Pacific, showcasing a wave train spanning across the North Pacific and an anticyclone over the eastern United States. The persistent wave train at week 0 also

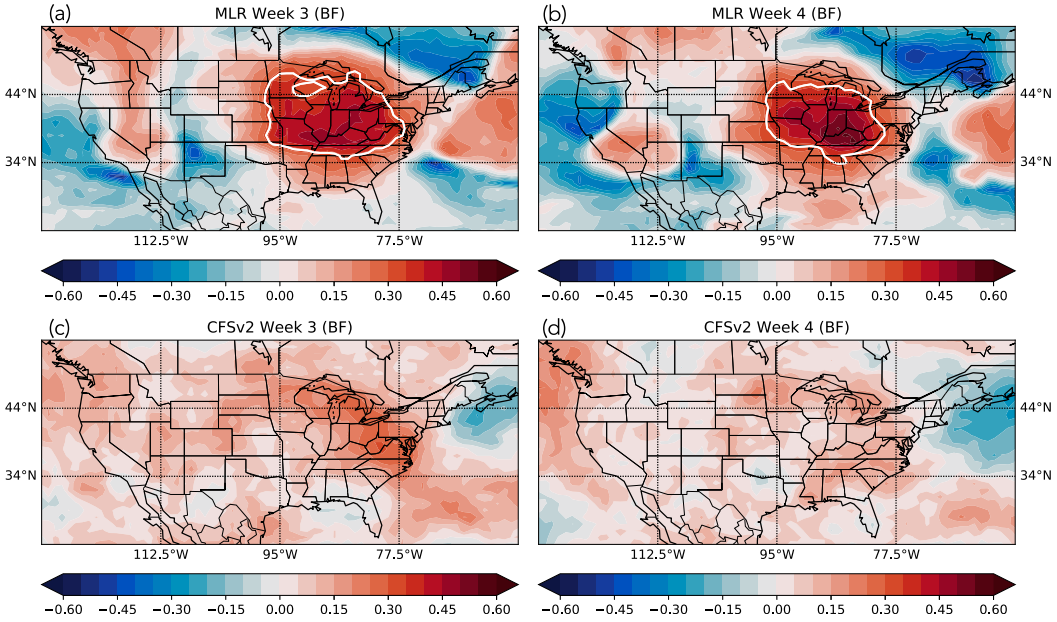

FIG. 6. As in Fig. 2, but for weekly blocking frequency.

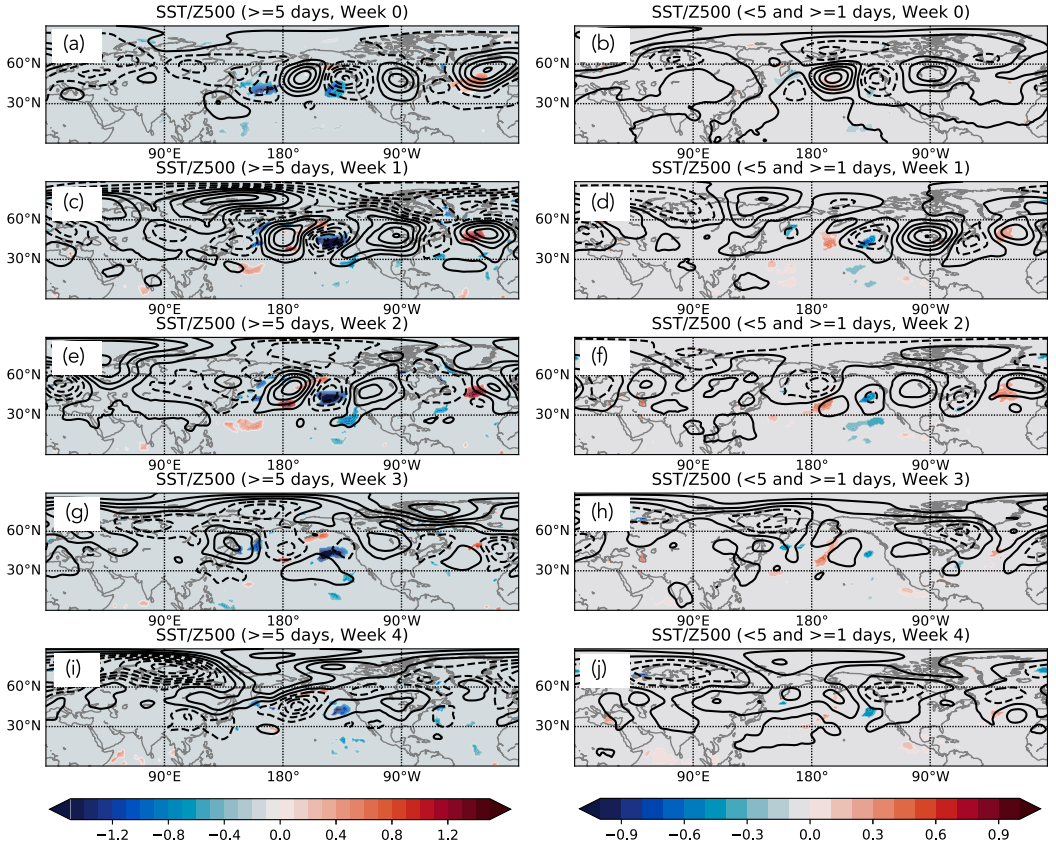

FIG. 7. (a),(c),(e),(g),(i) Composite differences of Z500 (contours from −150 to 150 m every 15 m) and SST (shading) based on when the WTZ500 index is extreme and persistent during week 0 (|WTZ500 index| > 1.0 standard deviation for at least 5 days during week 0). (b),(d),(f),(h),(j) Composite differences of Z500 (contours from −75 to 75 m every 15 m) and SST (shading) based on when the WTZ500 index is extreme but lasts less than 5 days during week 0 (|WTZ500 index| > 1.0 standard deviation for greater than 0 and less than 5 days during week 0). Week 0 is defined as from day −6 to day 0, whereas week 1 is defined as day 1–day 7. To prevent overlap, a persistent event cannot occur within 4 weeks of another event (10 events). Only significant differences of SST are shown ($\alpha = 0.05$). Note that the color-bar limits are different between the two columns.

showcases an extended waveguide over the Atlantic. An anomalous high is established over the eastern United States in week 1 and persists into week 3 for both groups. However, the wave train over the Pacific in the nonpersistent group weakens and no anticyclone is present at week 4. Previous studies (e.g., Ding and Wang 2005; Yasui and Watanabe 2010) suggested that diabatic heating in various regions (including the Indian summer monsoon) and the atmospheric internal dynamics both contribute to the circumglobal teleconnection pattern (CGT). Since the wave train pattern here slightly resembles the classic CGT pattern, it is possible that the wave train is excited by diabatic heating and atmospheric internal dynamics as well, and that a persistent wave train then induces SST anomalies over the North Pacific. Additionally, air–sea interaction and land–atmosphere interaction may help maintain the wave train (Teng et al. 2019). As shown in Fig. 8, persistent wave train events are associated with significantly reduced soil moisture anomalies in the eastern United States in week 1. The negative soil moisture anomalies persist in the following weeks. In contrast, the soil moisture anomalies for the nonpersistent WTZ500 events weaken with time and are far less coherent at week 4. The role of soil moisture anomalies is further examined in the next section.

b. *Soil moisture predictor*

Composites based on extreme values of the soil moisture index are examined in Fig. 9. Similar to the composites based on the NPSST index, the composites are constructed for days when the soil moisture index first becomes less than the 10th percentile (23 events over 1980–2017). The soil moisture anomalies resemble the second EOF at week 1 (Fig. 9a), with negative anomalies over the eastern United States and positive anomalies over the southern plains and Mexico (opposite anomalies of Fig. 1a), while a ridge is evident over the eastern United States. The negative soil moisture anomalies persist from week 1 to week 4 over the eastern United States, while the positive soil moisture anomalies weaken over the southern plains and Mexico. The anticyclone shifts southward from week 1 to week

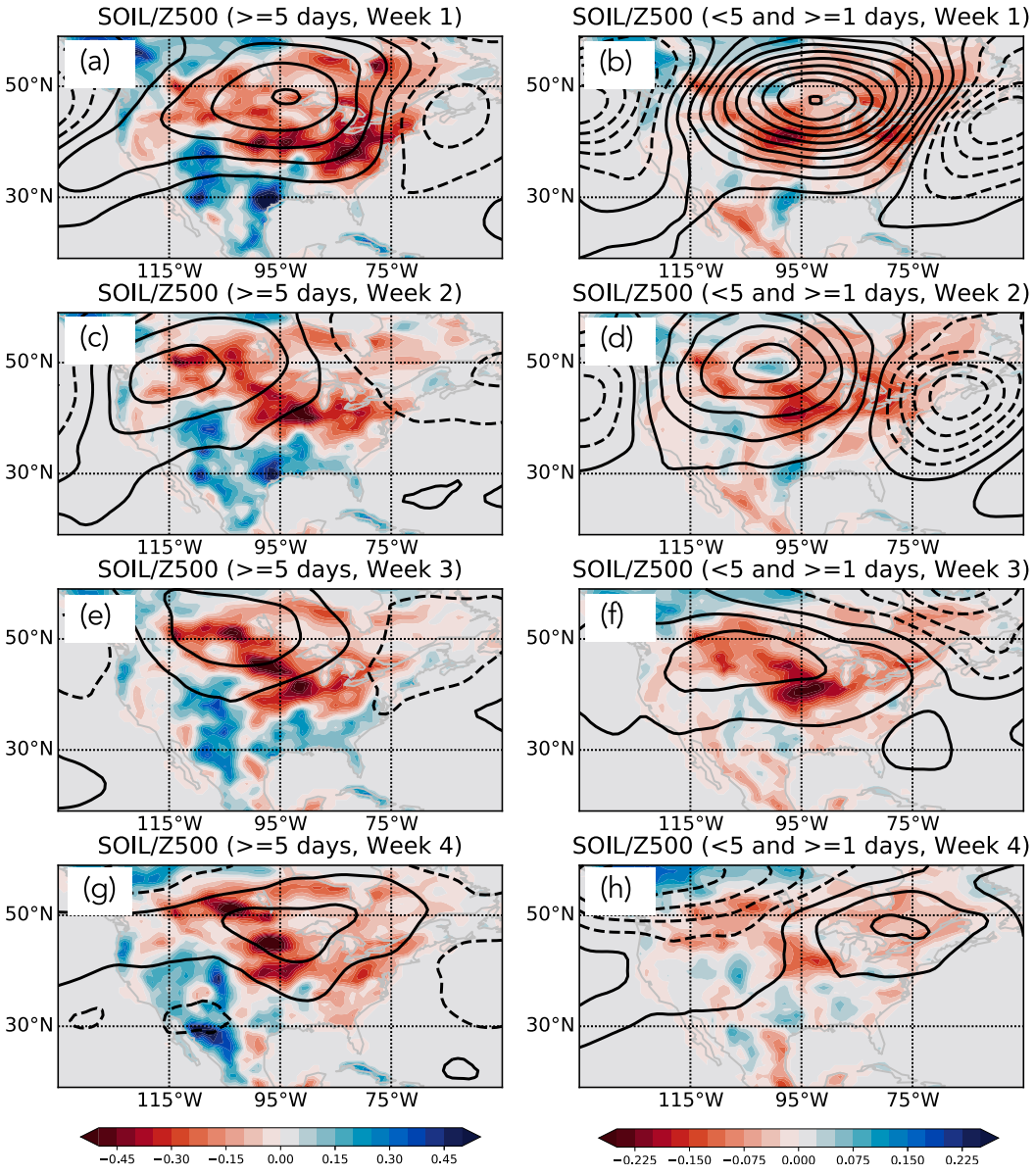

FIG. 8. As in Fig. 7, for but Z500 (contours) and volumetric soil moisture anomalies (shading). Note that the color-bar limits and contours are different between the two columns; for (a), (c), (e), and (g) the contours go from −150 to 150 m every 15 m and in (b), (d), (f), and (h) the contours go from −50 to 50 m every 10 m.

2 and weakens through week 3 and week 4 (Figs. 9a,d,g,j). Positive sensible heat flux anomalies are collocated with the strong negative soil moisture anomalies over the eastern half of the United States, which would aid in maintaining the anticyclone (Teng et al. 2019) and could contribute to the increase in blocking frequency (Figs. 9b,e,h,k). Laguë et al. (2019) showed an overall increase in sensible heat flux and solar radiation over the eastern United States due to reduced cloud cover when the evaporative resistance increases (or soil moisture decreases) in coupled model simulations. Regarding the weakening of the positive soil moisture anomalies over the southern plains and Mexico, it is likely due to the extension of the anticyclone into Mexico/Texas. In fact, this area experiences an increase in evaporation and a decrease in precipitation (not shown), both contributing to the diminishing soil moisture over Texas and Mexico.

A lagged relationship exists between the dry soil moisture and EWDs over the eastern United States (the right column in Fig. 9), as the anticyclone shifts southward over the eastern United States during the second week following dry soil moisture conditions. The anticyclone is associated with subsidence, reduced cloud cover, and increased solar radiation, and therefore an increase of EWDs at week 2 into week 4. The EWDs per week peak at week 3 (Fig. 9i) but are still significant

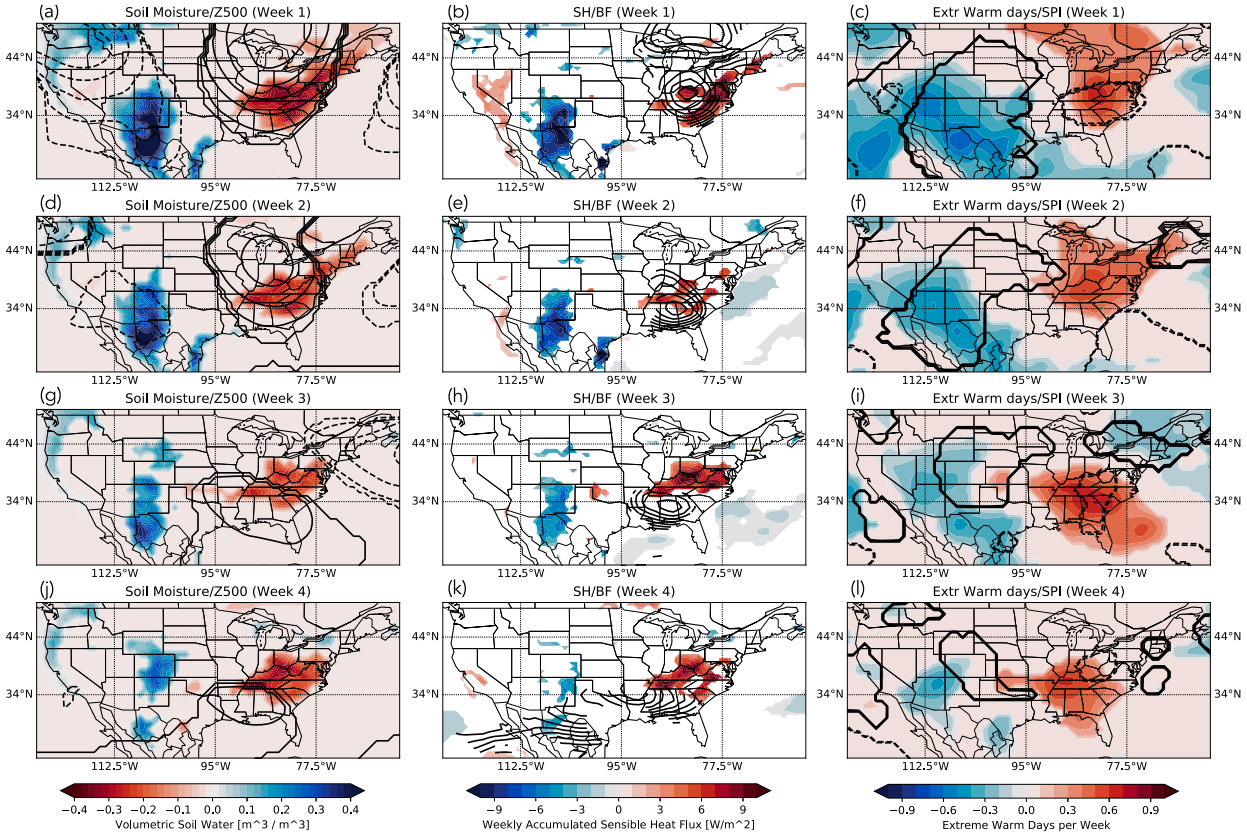

FIG. 9. Composite anomalies of (left) soil moisture (shading) and Z500 (contours from −100 to 100 m every 10 m), (center) sensible heat flux (shading) and blocking frequency (contours from −2 to 2 days every 0.25 days), and (right) extreme warm days per week (shading) and 14-day SPI (contours from −1 to 1 day every 0.25 days) at weeks (a)–(c) 1, (d)–(f) 2, (g)–(i) 3, and (j)–(l) 4 following extreme values of the soil moisture index. Composites are calculated based on when the soil moisture predictor first becomes less than the 10th percentile. To prevent overlap, an event cannot occur within 4 weeks of another event (23 events over 1980–2017). Only significant anomalies are shown ($\alpha = 0.05$).

at week 4 (Fig. 9l). The negative SPI values (low precipitation) are centered on the east coast of the United States, which is collocated with the negative soil moisture anomalies (left column), the increase in sensible heat flux (center column), and a decrease in evaporation (not shown).

5. Summary and conclusions

Despite the growing need for skillful prediction of extreme heat events at longer lead times, operational models produce far lower skill than desired beyond week 2. Therefore, we investigate statistical techniques to produce skillful predictions of EWDs and precipitation at lead times of 3–4 weeks. A North Pacific SST (NPSST) index and the second leading principal component of soil moisture over the United States are used to develop a multiple linear regression prediction model, and it demonstrates greater skill at weeks 3–4 than the Climate Forecast System, version 2 (CFSv2). As shown by composite analysis, the extreme values of the NPSST index are associated with a wave train that spans from the Eurasian continent to the North Atlantic, with a blocking anticyclone over the eastern United States that contributes to an increase of EWDs and negative SPI. Blocking frequency at weeks 3 and 4 can be predicted skillfully using the NPSST index as a predictor. Summer blocking events are difficult to predict as low-frequency climate modes, such as the MJO and ENSO, are weaker in summer than in winter. Further analysis showed that persistent wave train patterns are associated with strong SST anomalies over the North Pacific that project onto the second EOF mode of SST. It is likely that the NPSST index defined based on the EOF mode can be regarded as the footprint of persistent wave train events. However, more analysis is needed to understand the origin of the NPSST anomalies and the maintenance of the persistent wave train.

Composite analysis also suggests that the persistent circulation anomalies and increasing blocking occurrence over the eastern United States could also be attributed to positive land–atmosphere feedback. The increased blocking occurrence produces an increase in EWDs and low precipitation periods; reduced soil moisture leads to an increase in sensible heat flux and a decrease in latent heat flux, which help maintain a blocking high.

The two predictors discussed in this study provide skillful predictions on the subseasonal time scale. However, given the low-frequency nature of the predictors, it is possible that these

also operate on the interannual time scale (Vijverberg et al. 2020). Jong et al. (2021) demonstrated a statistically significant increase in surface temperature over the eastern United States during transitioning La Niña summers. The skill of our statistical model only decreases slightly after removal of the seasonal mean, indicating that subseasonal and interannual anomalies both contribute to the skillful predictions. One limitation is that this study is solely based on statistical analysis. Numerical model simulations, such as GCM experiments with prescribed SST or soil moisture, will help to further illustrate the underlying mechanisms and casual relationships.

The results of this study highlight the importance of SST and soil conditions in skillful long-range prediction of extreme heat events. It is important to reiterate that the predictors influence the occurrence of extreme heat events with a few weeks lag, and a statistical model like the one developed in this study can be used in conjunction with operational models at the shorter lead times as the operational forecast skill is much larger at week 1 and week 2. Recently, the authors demonstrated the importance and value of simple statistical and empirical models in predicting winter Eurasian atmospheric blocking (Miller and Wang 2019) and springtime U.S. severe weather (D. E. Miller et al. 2020). As with the previous studies, the MLR model here may serve as a benchmark for operational models at weeks 3 and 4 over the eastern United States while aiding in irrigation scheduling, crop planning, reservoir operation, and providing mitigation of impacts from extreme heat events.

Acknowledgments. This work is supported by the National Oceanic and Atmospheric Administration (NOAA) Grants NA18OAR4310271 and NA18NWS4680065. We acknowledge the NCAR Computational and Information Systems Laboratory (CISL) for providing computing resources. We thank Professor Ximing Cai for his discussions on the operational use of such models. We also thank the three anonymous reviewers for improving this paper.

Data availability statement. All ERAI data were provided and are available through the Research Data Archive (RDA; https://doi.org/10.5065/D6CR5RD9). The NCEP CFSv2 S2S model data are available online (https://apps.ecmwf.int/datasets/data/s2s-reforecasts-daily-averaged-kwbc/levtype=sfc/type=cf/).

REFERENCES

Adams, D. K., and A. C. Comrie, 1997: The North American monsoon. *Bull. Amer. Meteor. Soc.*, **78**, 2197–2213, https://doi.org/10.1175/1520-0477(1997)078<2197:TNAM>2.0.CO;2.

Alfaro, E. J., A. Gershunov, and D. Cayan, 2006: Prediction of summer maximum and minimum temperature over the central and western United States: The roles of soil moisture and sea surface temperature. *J. Climate*, **19**, 1407–1421, https://doi.org/10.1175/JCLI3665.1.

Balsamo, G., S. Boussetta, P. Lopez, and L. Ferranti, 2010: Evaluation of ERA-Interim and ERA-Interim-GPCP-rescaled precipitation over the U.S.A. ERA Rep. Series 5, 10 pp., https://www.ecmwf.int/en/elibrary/7926-evaluation-era-interim-and-era-interim-gpcp-rescaled-precipitation-over-usa.

Brunner, L., G. C. Hegerl, and A. K. Steiner, 2017: Connecting atmospheric blocking to European temperature extremes in spring. *J. Climate*, **30**, 585–594, https://doi.org/10.1175/JCLI-D-16-0518.1.

DeAngelis, A. M., H. Wang, R. D. Koster, S. D. Schubert, Y. Chang, and J. Marshak, 2020: Prediction skill of the 2012 U.S. Great Plains flash drought in subseasonal experiment (SubX) models. *J. Climate*, **33**, 6229–6253, https://doi.org/10.1175/JCLI-D-19-0863.1.

Dee, D. P., and Coauthors, 2011: The ERA-Interim reanalysis: Configuration and performance of the data assimilation system. *Quart. J. Roy. Meteor. Soc.*, **137**, 553–597, https://doi.org/10.1002/qj.828.

Diffenbaugh, N. S., J. S. Pal, F. Giorgi, and X. Gao, 2007: Heat stress intensification in the Mediterranean climate change hotspot. *Geophys. Res. Lett.*, **34**, L11706, https://doi.org/10.1029/2007GL030000.

Ding, Q., and B. Wang, 2005: Circumglobal teleconnection in the Northern Hemisphere summer. *J. Climate*, **18**, 3483–3505, https://doi.org/10.1175/JCLI3473.1.

Dole, R., and N. Gordon, 1983: Persistent anomalies of the extratropical Northern Hemisphere wintertime circulation: Geographical distribution and regional persistence characteristics. *Mon. Wea. Rev.*, **111**, 1567–1586, https://doi.org/10.1175/1520-0493(1983)111<1567:PAOTEN>2.0.CO;2.

Ferranti, L., S. Corti, and M. Janousek, 2015: Flow-dependent verification of the ECMWF ensemble over the Euro-Atlantic sector. *Quart. J. Roy. Meteor. Soc.*, **141**, 916–924, https://doi.org/10.1002/qj.2411.

Hirschi, M., and Coauthors, 2011: Observational evidence for soil-moisture impact on hot extremes in southeastern Europe. *Nat. Geosci.*, **4**, 17–21, https://doi.org/10.1038/ngeo1032.

Hoskins, B. J., A. J. Simmons, and D. G. Andrews, 1977: Energy dispersion in a barotropic atmosphere. *Quart. J. Roy. Meteor. Soc.*, **103**, 553–567, https://doi.org/10.1002/qj.49710343802.

Huang, J., H. M. van den Dool, and K. P. Georgakakos, 1996: Analysis of model-calculated soil moisture over the United States (1931–1993) and applications to long-range temperature forecasts. *J. Climate*, **9**, 1350–1362, https://doi.org/10.1175/1520-0442(1996)009<1350:AOMCSM>2.0.CO;2.

Jones, C., D. E. Waliser, K. M. Lau, and W. Stern, 2004: The Madden–Julian oscillation and its impact on Northern Hemisphere weather predictability. *Mon. Wea. Rev.*, **132**, 1462–1471, https://doi.org/10.1175/1520-0493(2004)132<1462:TMOAII>2.0.CO;2.

Jong, B.-T., M. Ting, and R. Seager, 2021: Assessing ENSO summer teleconnections, impacts, and predictability in North America. *J. Climate*, **34**, 3629–3643, https://doi.org/10.1175/JCLI-D-20-0761.1.

Koster, R. D., Y. Chang, and S. D. Schubert, 2014: A mechanism for land–atmosphere feedback involving planetary wave structures. *J. Climate*, **27**, 9290–9301, https://doi.org/10.1175/JCLI-D-14-00315.1.

——, ——, H. Wang, and S. D. Schubert, 2016: Impacts of local soil moisture anomalies on the atmospheric circulation and on remote surface meteorological fields during boreal summer: A comprehensive analysis over North America. *J. Climate*, **29**, 7345–7364, https://doi.org/10.1175/JCLI-D-16-0192.1.

Kumar, A., L. Zhang, and W. Wang, 2013: Sea surface temperature–precipitation relationship in different reanalyses. *Mon. Wea. Rev.*, **141**, 1118–1123, https://doi.org/10.1175/MWR-D-12-00214.1.

Laguë, M. M., G. B. Bonan, and A. L. Swann, 2019: Separating the impact of individual land surface properties on the terrestrial surface energy budget in both the coupled and uncoupled

land–atmosphere system. *J. Climate*, **32**, 5725–5744, https://doi.org/10.1175/JCLI-D-18-0812.1.

Li, M., P. Wu, and Z. Ma, 2020: A comprehensive evaluation of soil moisture and soil temperature from third-generation atmospheric and land reanalysis data sets. *Int. J. Climatol.*, **40**, 5744–5766, https://doi.org/10.1002/joc.6549.

Loikith, P. C., and A. J. Broccoli, 2014: The influence of recurrent modes of climate variability on the occurrence of winter and summer extreme temperatures over North America. *J. Climate*, **27**, 1600–1618, https://doi.org/10.1175/JCLI-D-13-00068.1.

Luo, M., and N.-C. Lau, 2020: Summer heat extremes in northern continents linked to developing ENSO events. *Environ. Res. Lett.*, **15**, 074042, https://doi.org/10.1088/1748-9326/ab7d07.

Lyon, B., and R. M. Dole, 1995: A diagnostic comparison of the 1980 and 1988 US summer heat wave-droughts. *J. Climate*, **8**, 1658–1675, https://doi.org/10.1175/1520-0442(1995)008<1658:ADCOTA>2.0.CO;2.

McKee, T., J. Doesken, and J. Kleist, 1993: The relationship of drought frequency and duration to time scales. *Proc. Eighth Conf. on Applied Climatology*, Anaheim, CA, Amer. Meteor. Soc., 179–184.

McKinnon, K. A., A. Rhines, M. P. Tingley, and P. Huybers, 2016: Long-lead predictions of eastern United States hot days from Pacific sea surface temperatures. *Nat. Geosci.*, **9**, 389–394, https://doi.org/10.1038/ngeo2687.

Meehl, G. A., and C. Tebaldi, 2004: More intense, more frequent, and longer lasting heat waves in the 21st century. *Science*, **305**, 994–997, https://doi.org/10.1126/science.1098704.

Miller, D. E., and Z. Wang, 2019: Skillful seasonal prediction of Eurasian winter blocking and extreme temperature frequency. *Geophys. Res. Lett.*, **46**, 11 530–11 538, https://doi.org/10.1029/2019GL085035.

——, ——, R. J. Trapp, and D. S. Harnos, 2020: Hybrid prediction of weekly tornado activity out to week 3: Utilizing weather regimes. *Geophys. Res. Lett.*, **47**, e2020GL087253, https://doi.org/10.1029/2020GL087253.

Miller, R. L., G. M. Lackmann, and W. A. Robinson, 2020: A new variable-threshold persistent anomaly index: Northern Hemisphere anomalies in the ERA-Interim reanalysis. *Mon. Wea. Rev.*, **148**, 43–62, https://doi.org/10.1175/MWR-D-19-0144.1.

Mueller, B., and S. I. Seneviratne, 2012: Hot days induced by precipitation deficits at the global scale. *Proc. Natl. Acad. Sci. USA*, **109**, 12 398–12 403, https://doi.org/10.1073/pnas.1204330109.

Namias, J., 1952: The annual course of month-to-month persistence in climatic anomalies. *Bull. Amer. Meteor. Soc.*, **33**, 279–285, https://doi.org/10.1175/1520-0477-33.7.279.

——, 1982: Anatomy of Great Plains protracted heat waves (especially the 1980 U.S. summer drought). *Mon. Wea. Rev.*, **110**, 824–838, https://doi.org/10.1175/1520-0493(1982)110<0824:AOGPPH>2.0.CO;2.

National Academies of Sciences, Engineering, and Medicine, 2016: *Next Generation Earth System Prediction: Strategies for Subseasonal to Seasonal Forecasts.* National Academies Press, 350 pp.

Orth, R., and S. I. Seneviratne, 2014: Using soil moisture forecasts for sub-seasonal summer temperature predictions in Europe. *Climate Dyn.*, **43**, 3403–3418, https://doi.org/10.1007/s00382-014-2112-x.

Pepler, A. S., L. B. Díaz, C. Prodhomme, F. J. Doblas-Reyes, and A. Kumar, 2015: The ability of a multi-model seasonal forecasting ensemble to forecast the frequency of warm, cold and wet extremes. *Wea. Climate Extremes*, **9**, 68–77, https://doi.org/10.1016/j.wace.2015.06.005.

Pfahl, S., and H. Wernli, 2012: Quantifying the relevance of atmospheric blocking for co-located temperature extremes in the Northern Hemisphere on (sub-) daily time scales. *Geophys. Res. Lett.*, **39**, L12807, https://doi.org/10.1029/2012GL052261.

Qin, J., and W. A. Robinson, 1995: The impact of tropical forcing on extratropical predictability in a simple global model. *J. Atmos. Sci.*, **52**, 3895–3910, https://doi.org/10.1175/1520-0469(1995)052<3895:TIOTFO>2.0.CO;2.

Saha, S., and Coauthors, 2014: The NCEP Climate Forecast System version 2. *J. Climate*, **27**, 2185–2208, https://doi.org/10.1175/JCLI-D-12-00823.1.

Seager, R., R. Murtugudde, N. Naik, A. Clement, N. Gordon, and J. Miller, 2003: Air–sea interaction and the seasonal cycle of the subtropical anticyclones. *J. Climate*, **16**, 1948–1966, https://doi.org/10.1175/1520-0442(2003)016<1948:AIATSC>2.0.CO;2.

Seneviratne, S. I., T. Corti, E. L. Davin, M. Hirschi, E. B. Jaeger, I. Lehner, B. Orlowsky, and A. J. Teuling, 2010: Investigating soil moisture–climate interactions in a changing climate: A review. *Earth-Sci. Rev.*, **99**, 125–161, https://doi.org/10.1016/j.earscirev.2010.02.004.

Slater, L. J., G. Villarini, and A. A. Bradley, 2019: Evaluation of the skill of North-American Multi-Model Ensemble (NMME) global climate models in predicting average and extreme precipitation and temperature over the continental USA. *Climate Dyn.*, **53**, 7381–7396, https://doi.org/10.1007/s00382-016-3286-1.

Teng, H., and G. Branstator, 2017: Connections between heat waves and circumglobal teleconnection patterns in the Northern Hemisphere summer. *Climate Extremes: Patterns and Mechanisms*, *Geophys. Monogr.*, Vol. 226, Amer. Geophys. Union, 177–193, https://doi.org/10.1002/9781119068020.ch11.

——, ——, G. A. Meehl, and W. M. Washington, 2016: Projected intensification of subseasonal temperature variability and heat waves in the Great Plains. *Geophys. Res. Lett.*, **43**, 2165–2173, https://doi.org/10.1002/2015GL067574.

——, ——, A. B. Tawfik, and P. Callaghan, 2019: Circumglobal response to prescribed soil moisture over North America. *J. Climate*, **32**, 4525–4545, https://doi.org/10.1175/JCLI-D-18-0823.1.

Tian, D., E. F. Wood, and X. Yuan, 2017: CFSv2-based sub-seasonal precipitation and temperature forecast skill over the contiguous United States. *Hydrol. Earth Syst. Sci.*, **21**, 1477–1490, https://doi.org/10.5194/hess-21-1477-2017.

Vijverberg, S., M. Schmeits, K. van der Wiel, and D. Coumou, 2020: Sub-seasonal statistical forecasts of eastern United States hot temperature events. *Mon. Wea. Rev.*, **148**, 4799–4822, https://doi.org/10.1175/MWR-D-19-0409.1.

Wilks, D. S., 2011: *Statistical Methods in the Atmospheric Sciences*. 3rd ed. Academic Press, 704 pp.

Yasui, S., and M. Watanabe, 2010: Forcing processes of the summertime circumglobal teleconnection pattern in a dry AGCM. *J. Climate*, **23**, 2093–2114, https://doi.org/10.1175/2009JCLI3323.1.